Materials Horizons

ROYAL SOCIETY OF CHEMISTRY

COMMUNICATION

View Article Online
View Journal

Cite this: DOI: 10.1039/d5mh01275a

Received 3rd July 2025,
Accepted 21st October 2025

DOI: 10.1039/d5mh01275a

rsc.li/materials-horizons

Method for measuring exciton–exciton annihilation rate constants in thermally activated delayed fluorescent emitters to understand efficiency roll-off in OLEDs

Le Zhang, †[ab] Arvydas Ruseckas,†*[a] Kou Yoshida,[a] Liam G. King,[a] Subeesh Madayanad Suresh,[b] Eli Zysman-Colman *[b] and Ifor D. W. Samuel *[a]

Efficiency roll-off at high luminance is a significant issue in organic light-emitting diodes (OLEDs) made using thermally activated delayed fluorescence (TADF) emitters. It is often attributed to singlet–triplet annihilation (STA) or triplet–triplet annihilation (TTA) in the light-emitting layer, but their contributions are not properly quantified because of uncertainty about the magnitude of the rate constants. Here we show that a combination of time-resolved photoluminescence (PL) measurements with variable pulse repetition rate and with background illumination provides a reliable method to study STA and TTA. We find that the STA rate constant in a multi-resonant TADF emitter DABNA-2 dispersed in mCBP increases from about 3×10^{-11} to 1×10^{-10} cm^3 s^{-1} with increasing emitter concentration from 3 to 10 wt%. The rate constant for TTA in the film with 10 wt% of DABNA-2 is four orders of magnitude smaller than that for STA and below the sensitivity limit at lower concentration of DABNA-2. Modelling of the OLED efficiency roll-off with experimentally determined parameters shows that STA is responsible for more than half of the efficiency loss at high luminance in the device with this emitter, whilst TTA can slightly reduce the effect of STA. The combination of these measurements and modelling is a powerful tool that can be employed for selecting the optimal host material for a particular emitter and the emitter concentration to minimize efficiency roll-off.

New concepts

TADF emitters can turn dark triplet states into emissive singlets and so achieve up to unity charge-to-photon conversion efficiencies in OLEDs. The conversion efficiency, however, decreases sharply with increasing luminance, especially in blue TADF and multi-resonant TADF OLEDs. Our understanding of this efficiency roll-off is limited by not knowing the rate constants of singlet–triplet annihilation and triplet–triplet annihilation and the difficulty of measuring them because of the dominance of singlet–singlet annihilation in optical measurements and the uncertainties in the triplet density profile in electroluminescence. Here we demonstrate a variable excitation repetition rate method to control the steady-state triplet density and so measure relevant rate constants using time-resolved fluorescence. Such measurements help to identify the processes limiting the OLED efficiency at high luminance and suggest ways to improve the efficiency roll-off by changing the composition of the light-emitting layer.

Introduction

Organic light-emitting diodes (OLEDs) are now widely used in displays across a range of consumer electronic devices. However, improving the efficiency of blue light emission remains a major materials challenge for the field. In OLEDs only 25% of the injected charges form emissive singlet excitons whilst the remaining 75% form triplet states, which in organic molecules are much less emissive because the transition to the ground state is spin-forbidden. Heavy metals can be used to enhance spin–orbit coupling and increase intersystem crossing and phosphorescence rates; in fact, iridium complexes are presently used as the emitters in the green and red subpixels in commercialized OLEDs. However, to date there is not a viable phosphorescent metal complex that produces blue devices with sufficient stability to satisfy industry standards. A very attractive alternative route to harvest triplet states is to exploit thermally activated delayed fluorescence (TADF), which occurs in molecules having a small energy gap between their lowest singlet and triplet excited states (S_1 and T_1 in Fig. 1) and is mediated by reverse intersystem crossing (RISC) from the triplet to the singlet manifold. The last decade has seen great progress in the development of TADF emitters for OLEDs.[1–3] Among them, multi-resonant TADF (MR-TADF) compounds attractively show narrowband emission (the full width at half maximum, FWHM, is typically less than 30 nm) and so address the required industry Rec. 2020 colour point criterion for

[a] Organic Semiconductor Centre, SUPA, School of Physics and Astronomy, University of St. Andrews, St. Andrews, KY16 9SS, UK. E-mail: ar30@st-andrews.ac.uk, idws@st-andrews.ac.uk

[b] Organic Semiconductor Centre, EaStCHEM School of Chemistry, University of St Andrews, St Andrews, KY16 9ST, UK. E-mail: eli.zysman-colman@st-andrews.ac.uk

† These authors contributed equally to this work.

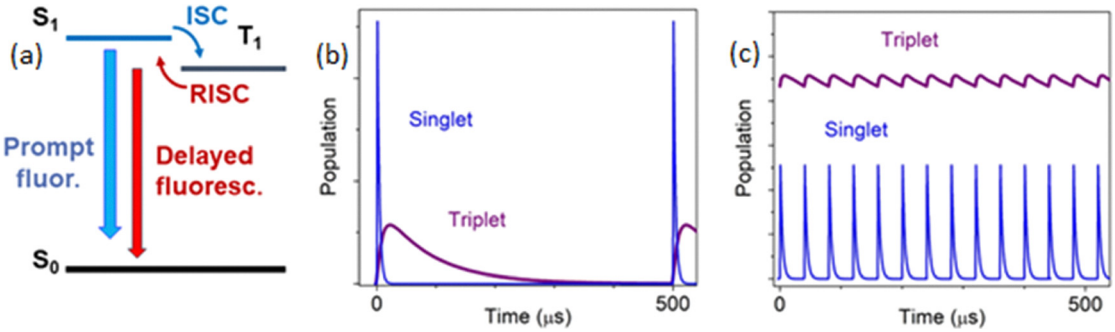

Fig. 1 (a) Schematic representing the photophysics of TADF: optically excited molecule in the singlet state S_1 can emit light as prompt fluorescence or cross to the triplet manifold by ISC to populate the T_1 state. For small energy gap between S_1 and T_1 states, ΔE_{ST}, the population of the T_1 state can cross back to the S_1 state by thermally activated RISC and emit delayed fluorescence. (b) Graph illustrating population of singlet and triplet states following pulsed excitation with a period between pulses longer than the triplet lifetime. (c) Graph illustrating the situation when the period between excitation pulses is shorter than the triplet lifetime and a well-defined quasi-steady-state triplet population builds up in the sample.

display applications.[4–6] The device efficiency, however, decreases sharply with increasing luminance, and this efficiency roll-off is especially strong in OLEDs with MR-TADF emitters. Recently, blue OLEDs with MR-TADF emitters have been reported to achieve external quantum efficiency (EQE) greater than 33% at low luminance.[7] However, when increasing the luminance to 1000 cd m^{-2} as required for use in displays for practical applications, the efficiency typically drops below 20%. There are some reports of blue TADF-sensitised fluorescent (hyperfluorescent) OLEDs where an EQE over 25% is retained at 1000 cd m^{-2}, but the stability is still much worse than that of green and red devices[7–9] so developing bright, efficient and stable blue OLEDs remains very challenging.

Several processes may contribute to the efficiency roll-off in OLEDs at high luminance, including singlet–triplet annihilation (STA), triplet–triplet annihilation (TTA), singlet-polaron quenching (SPQ), triplet-polaron quenching (TPQ), charge leakage, changes in charge carrier balance or light outcoupling, and Joule heating.[10–17] Previous studies have shown that STA, TTA, SPQ and TPQ occur in TADF OLEDs, but estimations of the individual rate constants for each of these processes vary over several orders of magnitude.[18–25] For example, a high STA rate constant, γ_{STA}, on the order of 10^{-9} cm^3 s^{-1} has been estimated in a device with the MR-TADF emitter *o*-Tol-*ν*-DABNA-Me at 3 wt% in DBFPO host.[7] Much lower γ_{STA} on the order of 10^{-12}–10^{-11} cm^3 s^{-1} have been measured in neat films of ACRXTN[21] and CzDBA.[24] The reported TTA rate constants γ_{TTA} vary between 10^{-17} and 10^{-11} cm^3 s^{-1}, albeit the lowest value was measured at a low temperature of 6.5 K.[26] Such a wide spread of the rate constants suggests large variation in exciton diffusion, which mediates STA and TTA, and points to the need for more reliable measurements, so that materials can be developed for brighter, more efficient, and more stable OLEDs.

Here we demonstrate a method to study STA and TTA in TADF emitters by varying the repetition rate of the excitation pulses f_{rep}. When the period between the excitation pulses $T_{rep} = \frac{1}{f_{rep}}$ is much longer than the lifetime of the triplet excitons, all triplet excitons decay through TADF or non-radiatively before the arrival of the next excitation pulse (Fig. 1b). In contrast, a well-defined quasi-steady-state population of triplet excitons builds up when using T_{rep} shorter than the triplet lifetime (Fig. 1c). By varying f_{rep} we can change the triplet population and so measure its effect on the prompt emission to deduce the γ_{STA} in combination with the measurement of delayed fluorescence at varying excitation fluence. This helps to overcome the limitations of time-resolved PL measurements at low pulse repetition rates where the triplet population is very small, and the decays are dominated by singlet–singlet annihilation. To illustrate the method, we apply it to the MR-TADF emitter DABNA-2 in films at different concentrations in the mCBP host and model the efficiency roll-off of devices with this emitter using experimentally determined parameters to give new insight into the roll-off mechanisms.

Results and discussion

Steady-state and time-resolved photoluminescence

Films of DABNA-2 at a range of concentrations in mCBP host were prepared by co-evaporation. Fig. 2 shows the absorbance and normalised PL spectra. The absorbance at 450 nm is attributed to the short-range charge-transfer $S_0 \rightarrow S_1$ electronic transition in DABNA-2 and is low because of the low concentration of the emitter in the films. The peak position in the PL spectra, λ_{PL}, at 468 nm does not shift with concentration of DABNA-2, which indicates that the nature of the emitting state does not change for this concentration range. The PL quantum yield (PLQY) of these films is ~80%, which is similar to the values previously reported in the same host.[27]

These films show a delayed fluorescence lifetime, τ_d, of *ca.* 100 μs, which can be used as a lower bound of the triplet lifetime in DABNA-2 (Fig. S1 in SI). In order to test the distribution of DABNA-2 molecules in blend films, we excited the mCBP host at 343 nm and measured the kinetics of electronic energy transfer from mCBP to DABNA-2 by time-resolved PL (Fig. S2 in SI). Nearly mono-exponential decays of the mCBP emission and a corresponding rise of the DABNA-2 emission are observed. The results indicate

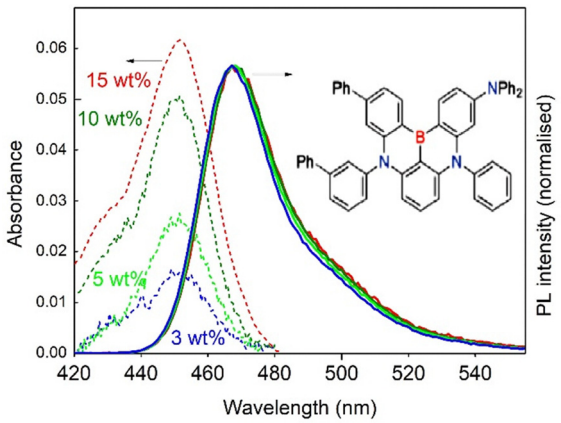

Fig. 2 Absorbance (dashed lines) and normalized PL (λ_{exc} = 375 nm) spectra of DABNA-2 dispersed in mCBP host at different concentrations in wt%. The inset shows the molecular structure of DABNA-2.

homogeneous distribution of DABNA-2 molecules in the mCBP host matrix.

To study STA we need sufficiently high triplet exciton density in DABNA-2. We used 343 nm excitation for which ~35% of the incident light is absorbed in the film. Then we adjusted the excitation pulse energy so that the decay of the prompt fluorescence from DABNA-2 is not strongly affected by singlet–singlet annihilation (SSA). The PL kinetics measured at f_{rep} = 2 kHz and the incident pulse density of 5 μJ cm^{-2} and 10 μJ cm^{-2} are nearly identical which shows that SSA has no significant influence at this pulse density (Fig. S3 in SI).

Using a fixed fluence of 5 μJ cm^{-2} at 343 nm but increasing the repetition rate of excitation pulses, f_{rep}, we observe faster decays of the prompt fluorescence of DABNA-2 (Fig. 3a). When the period between the excitation pulses is shorter than the triplet exciton lifetime of ~100 μs, a quasi-steady-state population of triplet excitons exists and causes fluorescence quenching by energy transfer from singlet to triplet excitons. This transfer populates a higher triplet state T_n, which usually relaxes back to T_1 unless it undergoes a photochemical reaction. As a result, one singlet exciton is lost per STA event, leaving a triplet exciton, *i.e.*, $S_1 + T_1 \rightarrow S_0 + T_n \rightarrow S_0 + T_1$. Control measurements at the same excitation spot at 2 kHz after measurements at 200 kHz were carried out to check for possible photodegradation. In all samples the same PL kinetics are reproduced after exposure, indicating that the sample fully recovers after exposure to the excitation with 10 μJ cm^{-2} at 200 kHz. The faster decay of the prompt fluorescence at high f_{rep} (50, 100 and 200 kHz) indicates quenching by the accumulated triplet excitons.

Data analysis

The time-dependent densities of singlets N_S and triplets N_T under optical excitation are described by the rate equations

$$\frac{dN_S}{dt} = G - (k_S + k_{ISC} + \gamma_{STA}N_T)N_S + k_{RISC}N_T + 0.25\gamma_{TTA}N_T^2 \quad (1)$$

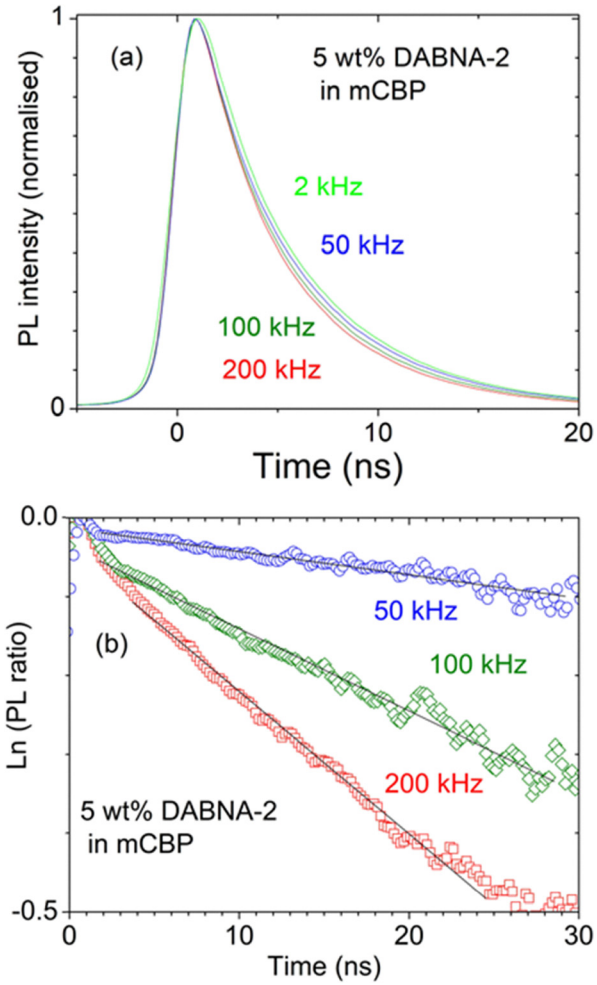

Fig. 3 (a) Kinetics of the DABNA-2 prompt fluorescence in film with 5 wt% of DABNA-2 in mCBP measured with varying f_{rep} of excitation pulses at 343 nm at an incident pulse density of 5 μJ cm^{-2}. (b) Natural logarithm of the PL ratio = I(high f_{rep})/I(2 kHz) (symbols) and fits to eqn (3) (solid lines).

$$\frac{dN_T}{dt} = k_{ISC}N_S - (k_{RISC} + k_T)N_T - 1.25\gamma_{TTA}N_T^2 \quad (2)$$

Here G is the generation function, k_S and k_T are the decay rate constants of singlet and triplet excitons to the ground state, the rate constants k_{ISC} and k_{RISC} describe ISC and RISC and are obtained from PLQY and time-resolved PL measurements as described in SI. We did not include SSA in these rate equations because it has no significant influence on the PL kinetics at the incident pulse density up to 10 μJ cm^{-2}. We assumed that TTA generates singlet and triplet excitons with a 1 : 3 ratio. By spin statistics, TTA can generate singlet, triplet and quintet states with 1 : 3 : 5 ratio. However, much higher singlet exciton yields have been reported in organic semiconductors which suggests that the quintet state is not energetically accessible or unstable and dissociates back into two triplets leading to 1 : 3 or even higher singlet–triplet ratio.[28]

In the prompt fluorescence regime, the RISC and TTA contributions are negligible, therefore, the quenching rate by STA can be directly determined from eqn (1) by taking the ratio

of the time-resolved fluorescence intensities measured at the high and low f_{rep}, *i.e.*, PL ratio = I(high f_{rep})/I(2 kHz), as this divides out other decay channels of singlet excitons. We find that quenching by triplets at $t > 3$ ns can be well approximated to a mono-exponential decay which indicates that the quenching rate is defined by the time it takes for singlet exciton to diffuse to the quencher (Fig. 3b). The faster quenching component at $t < 3$ ns with a smaller amplitude is attributed to the direct Förster resonance energy transfer (FRET) to triplets which are within the Förster radius from photogenerated singlets. The amplitude of the fast component increases at 200 kHz because of higher triplet density, so that a larger fraction of singlet excitons can transfer energy directly to triplets. This effect is more pronounced when using a higher pulse density of 10 μJ cm^{-2} which also generates more triplets as shown in Fig. S4 in SI. Similar behaviour has been observed for fluorescence quenching by injected polarons in polyfluorene films.[16]

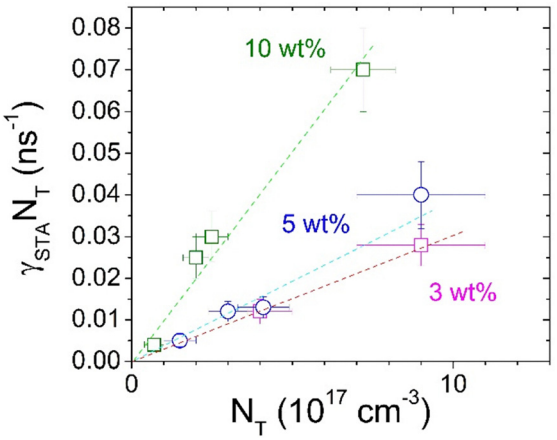

Fig. 4 Rate constant of PL quenching *vs.* steady state triplet density N_T determined using the data shown in Fig. 3, Fig. S4 and S6. The dashed lines are linear fits used for determining γ_{STA}.

Determination of γ_{TTA} and γ_{STA}

The main component of PL quenching by STA can be described by

$$\frac{I(\text{high}\, f_{rep})}{I(2\,\text{kHz})} = g_0 \exp(-\gamma_{STA} N_T t) \quad (3)$$

where g_0 is the scaling factor of fluorescence intensities and N_T is the accumulated quasi steady-state density of triplet excitons. The estimation of N_T is the key to further analysis. In the steady-state regime $\frac{dN_S}{dt} = \frac{dN_T}{dt} = 0$ and $G = N_0 f_{rep}$, where N_0 is the density of singlet excitons generated by a single excitation pulse determined as the number of absorbed photons per excitation volume. The incident pulse density of 5 μJ cm^{-2} at 343 nm gives $N_0 = 3 \times 10^{17}$ cm^{-3} (details given in the SI). To evaluate the effect of TTA on the steady-state triplet density we varied γ_{TTA} values from 10^{-17} to 10^{-11} cm^3 s^{-1} and calculated N_T (200 kHz), N_T (50 kHz), and their ratio, which are shown in Fig. S5 in SI. To include the weak effect of SSA on the steady-state triplet population we used the apparent singlet decay rates k_S measured with the same pulse density as in STA measurements but at 2 kHz where STA is negligible. The calculation shows that for $\gamma_{TTA} < 10^{-15}$ cm^3 s^{-1} the TTA effect on the steady-state N_T is very weak and their ratio r = N_T (200 kHz)/N_T (50 kHz) ≈ 3.5 is close to the ratio of four of the pulse repetition rates at 200 and 50 kHz. As γ_{TTA} increases, the ratio, r, decreases sharply and reaches $r = 2$ at $\gamma_{TTA} \approx 10^{-13}$ cm^3 s^{-1}. This is the classical multistep-diffusion-assisted TTA limit where the triplet exciton density at infinity follows the square root dependence on the exciton generation (pulse repetition) rate.[29]

Because the effect of TTA on the accumulated triplet density N_T in the steady-state regime is very weak for $\gamma_{TTA} < 10^{-15}$ cm^3 s^{-1}, we first considered γ_{TTA} in the range 10^{-15}–10^{-13} cm^3 s^{-1}. For each value of γ_{TTA} we calculated the triplet density and determined the range of γ_{STA} values using the linear fits in Fig. 4. We then measured the delayed fluorescence lifetime of DABNA-2 in the films using the frequency-domain technique under background illumination by a continuous wave (CW) 450 nm laser diode to generate a large triplet population.[30] By solving the coupled rate eqn (1) and (2) and fitting to the delayed fluorescence lifetime data, we were able to refine the value of γ_{TTA} as shown in Fig. S6a in SI. We then used this refined value of γ_{TTA} to calculate the refined triplet density and γ_{STA}. Such an approach was necessary as γ_{TTA} determines the triplet density and affects the value of γ_{STA}. Based on this process, we obtain a best-fit of $\gamma_{TTA} = 1.3 \times 10^{-14}$ cm^3 s^{-1} for 10 wt% DABNA-2: mCBP which gives us $\gamma_{STA} = 1.0 \times 10^{-10}$ cm^3 s^{-1}. By fitting the data for 5 wt% DABNA-2: mCBP in Fig. S6b we determine an upper limit of 10^{-14} cm^3 s^{-1} for γ_{TTA}. Based on this information, taking γ_{TTA} between 0 and its upper limit of 10^{-14} cm^3 s^{-1} results in a γ_{STA} value in the range of 4×10^{-11} to 6×10^{-11} cm^3 s^{-1} for 5 wt% DABNA-2: mCBP. As a further check that the upper limit is reasonable, we considered triplet diffusion in DABNA-2 by an electron exchange mechanism. Because γ_{TTA} is approximately proportional to the triplet diffusion coefficient, its value in 5 wt% DABNA-2 film is predicted to be at least ten times lower than in the 10 wt% film (details in SI). Using the same upper limit of $\gamma_{TTA} < 10^{-14}$ cm^3 s^{-1} for 3 wt% DABNA-2: mCBP gives γ_{STA} in the range of 2.5×10^{-11} cm^3 s^{-1} to 4×10^{-11} cm^3 s^{-1}.

As mentioned in the Introduction, previously reported γ_{TTA} values of TADF emitters lie within a very wide range from 10^{-17} to 10^{-11} cm^3 s^{-1}, which motivated us to develop more reliable measurements. The highest value $\gamma_{TTA} = 1.3 \times 10^{-14}$ cm^3 s^{-1} we obtained for 10 wt% DABNA-2: mCBP is lower by one order of magnitude than the reported value in the neat films of the green TADF emitter ACRXTN[21] and by two orders of magnitude lower than reported in a neat film of another green TADF emitter CzDBA.[24] These results are consistent with shorter intermolecular spacing in neat films. An extremely low γ_{TTA} of 5×10^{-18} cm^3 s^{-1} was reported for another TADF emitter 4CzIPN dispersed at 10 wt% in mCP host, but this was measured at 6.5 K.[26] This small value is likely to be the result of hindered triplet diffusion at this low temperature because

excitons become trapped at low-energy sites and their release is slow. It is interesting to note that the γ_{TTA} values for DABNA-2 are lower than those of *fac*-Ir(ppy)$_3$-cored dendrimers by an order of magnitude with the comparable centre-to-centre distance between them.[31] The difference can be explained by a significant contribution of dipole–dipole interactions to TTA in *fac*-Ir(ppy)$_3$ -cored dendrimers and/or stronger through-bond electron exchange interaction in dendrimers.

Our value of γ_{STA} for 3 wt% DABNA-2 film is similar to the STA rate constant reported for the neat film of CzDBA (2.5×10^{-11} cm^3 s^{-1})[24] but higher than the neat film of ACRXTN (on the order of 10^{-12} cm^3 s^{-1}).[21] Faster STA in films with DABNA-2 can be explained by its higher radiative rate constant $k_r = 1.4 \times 10^8$ s^{-1} as compared to ACRXTN ($k_r = 9 \times 10^6$ s^{-1})[21] and larger overlap of its emission and absorption spectra. High k_r induces strong dipole–dipole interactions between molecules and enhances singlet exciton diffusion and energy transfer to triplets by FRET. High k_r in TADF emitters is an obvious advantage for fast photon emission from the singlet state before it crosses to the triplet by ISC,[32] but it also enhances STA at high triplet density.

We can estimate the triplet diffusion coefficient D_T using the Smoluchowski equation $\gamma_{TTA} = 5\pi D_T R_a$, where R_a is the annihilation radius. Here we assumed the singlet–triplet ratio of 1 : 3 per TTA event. Using $R_a = 3.1$ nm which corresponds to an average spacing of DABNA-2 molecules at 5 wt% in mCBP and $\gamma_{TTA} < 1 \times 10^{-14}$ cm^3 s^{-1} we get $D_T < 2 \times 10^{-9}$ cm^2 s^{-1}. Similarly, $\gamma_{STA} = 4\pi(D_S + D_T)R_a$ and $\gamma_{STA} \approx 6 \times 10^{-11}$ cm^3 s^{-1} for 5 wt% DABNA-2 film gives the singlet diffusion coefficient $D_S \approx 1.6 \times 10^{-5}$ cm^2 s^{-1} and the singlet diffusion length $\sqrt{6\tau_S D_S} \approx 7$ nm for $\tau_S = 5.4$ ns. This indicates that STA can be significant at the triplet density of 10^{17} cm^{-3} and higher in the 5 wt% DABNA-2 films.

Efficiency roll-off in OLEDs

To investigate the effect of STA and TTA on efficiency roll-off of DABNA-2 OLEDs, we fabricated OLEDs with 5 wt% DABNA-2:mCBP as the light-emitting layer (EML) and diphenyl-4-triphenylsilylphenyl-phosphine oxide (TSPO1 OLED) as electron transport layer, which has a similar device structure as reported by Hatakeyama and coworkers[4] (see OLED fabrication in Experimental for the details). To check the effect of charge balance on the roll off, we also fabricated the OLED with the same EML but with an n-doped electron transport layer based on the cesium-doped 4,7-diphenyl-1,10-phenanthroline (BPhen) layer (BPhen:Cs OLED). Fig. 5 shows EQE of the OLEDs as a function of current density. EQEs and their roll-off characteristics of TSPO1 OLED and BPhen:Cs OLED are similar, so the charge balance does not have strong effect on EQE roll-off characteristics. We used the measured rate constants from the time-resolved PL studies to calculate the average exciton densities and the EQE roll-off as described in SI. First, we simulated the EQE roll-off assuming the width of the recombination zone $w = 20$ nm which is the thickness of the light emitting layer and found that the predicted EQE roll-off by STA is not as severe as experimentally observed (Fig. S7 in SI).

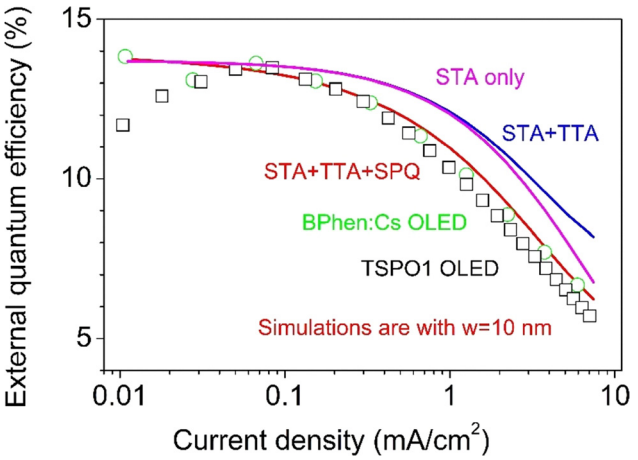

Fig. 5 Experimental EQE of OLEDs with 5 wt% DABNA-2:mCBP light emitting layer and different electron transport layers, TSPO1 (black squares) and BPhen:Cs (green circles) Lines show the simulated EQE using the measured rate constants $\gamma_{STA} = 6 \times 10^{-11}$ cm^3 s^{-1} and $\gamma_{TTA} = 1 \times 10^{-15}$ cm^3 s^{-1}, and assuming $\gamma_{SPQ} = \gamma_{STA}$. The closest fit to the experiment is obtained for the width of the recombination zone $w = 10$ nm.

We next considered quenching of singlets by charges (polarons) in the light-emitting layer. Charge carrier transport in disordered organic semiconductors is accelerated by the applied electric field along its direction. However, the rate of electron–hole recombination in OLEDs is limited by carrier diffusion in directions perpendicular to the electric field, and is likely to be controlled by the zero-field electron and hole mobilities μ_{0e} and μ_{0h}, respectively.[33,34] To estimate carrier mobilities we fabricated single-carrier devices having different DABNA-2 concentrations doped in mCBP. The current density in electron-only devices (EODs) and hole-only devices (HODs) decreased with the introduction of DABNA-2 into the mCBP host (Fig. S8 in SI). This indicates that both types of carriers get trapped by DABNA-2 as expected, because the ionization energy for DABNA-2 (5.38 eV) is substantially lower than that of mCBP (6.07 eV)[4] whilst electron affinity is higher (2.75 and 2.55 eV for DABNA-2 and mCBP, respectively). By fitting the current–voltage dependence in EODs to a space-charge limited current model we estimated the zero-field carrier mobility and the Poole–Frenkel factor (Table S1 in SI). Using the Einstein–Smoluchowski equation for diffusion of charged particle $D_p = \frac{\mu_e k_B T}{e}$ and $\mu_{0e} = 3 \times 10^{-8}$ cm^2 V^{-1} s^{-1} found in the film with 5 wt% of DABNA-2 we estimated the diffusion coefficient of polarons $D_p \approx 1 \times 10^{-9}$ cm^2 s^{-1}. It is four orders of magnitude smaller than that of singlets which we determined by STA indicating that polarons are much less mobile than singlet excitons – meaning SPQ and STA are both limited by singlet exciton diffusion.

Using the Langevin equation to calculate the average charge pair density in the light-emitting layer and the same rate constant for SPQ that we found for STA ($\sim 6 \times 10^{-11}$ cm^3 s^{-1}), we included SPQ into the EQE roll-off model. When the width of the recombination zone is reduced to 10 nm we get a good agreement with experiment (Fig. 5). Lower recombination width than the actual EML thickness is reasonable because the mCBP

is a hole conductive host and recombination will be expected to mainly happen near the interface between EML and TSPO1. According to the simulations, SPQ is the dominant efficiency roll-off mechanism for the current below 1 mA cm^{-2} whilst STA dominates at higher current. Despite an indication that TTA can reduce STA losses at high current, it is better to avoid both annihilation processes as they populate a higher energy triplet state at least for a short time and are likely to contribute to device degradation. Extending the width of the recombination zone by balancing charge injection and transport is important for reducing the triplet density and mitigating the detrimental STA and TTA processes. In order to reduce SPQ, the Langevin recombination rate must be increased, which requires higher electron and hole mobilities in the light-emitting layer. This indicates the need for better host materials for DABNA-2 emitter with suitable energy levels to reduce carrier trapping by DABNA-2.

Conclusions

We have shown that a combination of optical pulsed excitation at variable repetition rate and background illumination provides a reliable method to measure the rate constants for STA and TTA. These rate constants are important for identifying the efficiency-limiting processes in TADF OLEDs at high luminance. We found that the STA rate constant of 1×10^{-10} cm^3 s^{-1} measured in films with 10 wt% DABNA-2 is slightly higher than reported for some charge-transfer type TADF emitters. This can be explained by higher radiative rate constant of DABNA-2 and larger overlap of its emission and absorption spectra, both of which enhance FRET to triplets and singlet exciton diffusion mediating STA.

We showed that STA is a dominant efficiency loss mechanism in OLEDs with DABNA-2 emitter at high current, whilst the TTA effect is weak. We expect STA to be important for other MR-TADF emitters because of their high radiative rate constant and slow RISC. Our method will also be useful to study hyperfluorescent TADF systems where FRET to the triplets on the sensitiser can compete with light emission because of generally high radiative rate constants of fluorescent terminal emitters. Time-resolved PL measurements can be very effective tool for concentration optimisation of the terminal emitter as well as the sensitiser.

The variable excitation repetition rate method can be used with low average laser power, so it can be extended to study emitters with short delayed fluorescence lifetimes ($\tau_d < 5$ μs) using the excitation repetition rate in the MHz range. STA measurements in these emitters could be useful to explore their potential for applications in high peak power pulsed organic light sources.

Experimental

Film fabrication

DABNA-2 was synthesized according to the reported method,[4] sublimed mCBP was purchased from Lumtec. Thin films with concentrations of DABNA-2 of 3 wt%, 5 wt%, 10 wt%, and 15 wt% dispersed in mCBP host were fabricated by co-evaporation on fused silica substrates under a high vacuum with the base pressure less than 10^{-6} mbar (Angstrom evaporator, EvoVac PVD Platform, located inside a standard glove box). The final film thickness was 50 nm and monitored by a quartz crystal microbalance (QCM) during the evaporation. All substrates were cleaned by sonication in acetone for 15 min, IPA for 15 min, and then treated under oxygen plasma for 3 min. For time-resolved PL measurements samples were encapsulated in a glove box (O_2, $H_2O < 1$ ppm).

Basic optical characterization

Steady-state absorption and PL spectra were measured using a Varian Cary 300 spectrophotometer and Edinburgh Instruments fluorimeter FLS980, respectively. The excitation wavelength (λ_{exc}) for the PL measurement was 375 nm, and was generated by a pulsed laser diode (Picoquant, PLS 370). The photoluminescence quantum yield (PLQY) of the thin films was measured using an integrating sphere (Hamamatsu C9920-02, λ_{exc} = 345 nm) under a N_2 atmosphere. All measurements were conducted at room temperature.

Time-resolved photoluminescence spectroscopy

Energy transfer from mCBP to DABNA-2 was measured with a Hamamatsu streak camera in the synchroscan mode using the 3rd harmonic of a Pharos laser (Light Conversion) for excitation at 343 nm, pulse length 200 fs. Then the same excitation and camera were used with a slow sweep unit to study singlet–triplet annihilation (STA) in DABNA-2 emitters. In this experiment the incident pulse density was adjusted to minimise singlet–singlet annihilation and kept at $\leq$10 μJ cm^{-2}. The repetition rate of the excitation pulses, f_{rep}, was varied using the electro-optical pulse picker of Pharos laser. The decay time of prompt fluorescence at a low pump fluence of 0.5 μJ cm^{-2} at λ_{exc} = 375 nm was measured by time-correlated single photon counting (TCSPC, Edinburgh Instruments FLS980,). Measurements of delayed fluorescence were made by multi-channel scaling (MCS, Edinburgh Instruments FLS980, λ_{exc} = 375 nm).

Measurement of γ_{TTA}

The background illumination using a CW 450 nm laser diode with adjustable intensity was used to generate a large triplet exciton density in the DABNA-2: mCBP films. The reduction in the delayed fluorescence lifetime was measured by the frequency-domain photoluminescence technique using a modulated 450 nm laser diode for excitation.[30]

OLED fabrication

OLEDs were fabricated by thermally evaporating materials in the same vacuum chamber as the film fabrication. Precleaned 1.1 mm thick glass substrates with 117-nm-thick and pre-patterned ITO anodes (Xin Yan Technology Ltd) were treated with oxygen plasma. The substrates were then spin-coated with PEDOT:PSS (Heraeus Clevios, Al4800), diluted with deionized water in a 1 : 2 volume ratio, at 3000 rpm and baked at 150 °C for 10 min. The PEDOT:PSS layer was used to prevent shorting.

The organic layers consisted of 40-nm-thick *N*,*N*′-bis(naphthalen-1-yl)-*N*,*N*′-bis(phenyl)benzidine (NPB), 10-nm-thick tris(4-carbazoyl-9-ylphenyl)amine (TCTA), 10-nm-thick 1,3-bis(carbazol-9-yl)benzene (MCP), 20-nm-thick DABNA-2 doped at 5 wt% into mCBP, and 10-nm-thick diphenyl-4-triphenylsilylphenyl-phosphine oxide (TSPO1) were sequentially evaporated. To investigate the effect of electron injection on EQE-roll off characteristics, OLEDs with two different types of electron transport layers (ETLs) were fabricated. Additional 30-nm-thick TSPO1 layer and 2-nm-thick 8-quinolinolato lithium (Liq) as ETLs were evaporated and the OLED was termed as TSPO1 OLED. For other OLED batch we used a 40-nm-thick cesium-doped as BPhen as the ETL and the OLED was termed as BPhen:Cs OLED. Stronger electron injection is expected for the BPhen:Cs OLEDs than the TSPO1 OLEDs. Finally, 150-nm-thick aluminum was evaporated as cathode. All organic materials except DABNA-2 were purchased from commercial suppliers, Luminescence Technology Corp. or Ossila Ltd., and used as received. The active area of the OLEDs was 2 mm^2. After the evaporation process, the OLEDs were encapsulated under a nitrogen atmosphere using 1.1 mm thick custom-made cavity glass lids (Luminescence Technology Corp.), an epoxy glue (Norland Products Inc., Norland Optical Adhesive 68) pre-baked under a nitrogen condition, and a moisture getter (Dynic Corporation, HD-071210T-50S). The complete OLED structures were:

TSPO1 OLED: glass/ITO(117 nm)/PEDOT:PSS(<10 nm)/NPB(20 nm)/TCTA(10 nm)/MCP(10 nm)/5wt%-DABNA-2:mCBP (20 nm)/TSPO1(40 nm)/Liq(2 nm)/Al(150 nm),

BPhen:Cs OLED: glass/ITO(117 nm)/PEDOT:PSS(<10 nm)/NPB(20 nm)/TCTA(10 nm)/MCP(10 nm)/5 wt%-DABNA-2:mCBP (20 nm)/TSPO1(10 nm)/BPhen:Cs(40)/Al(150 nm).

EQE measurement

The current density–voltage–luminance (*J*–*V*–*L*) characteristics were tested using a source measure unit (Keithley Instruments, Keithley 2400) and a calibrated custom-made silicon photodiode module, with its output voltage measured with a multimeter (Keithley Instruments, Keithley 2000). The external quantum efficiency (EQE) of the OLEDs was estimated assuming a Lambertian emission pattern. Emission spectra were measured using a calibrated fiber-coupled spectrograph (MS125, Oriel) equipped with a charge-coupled device (CCD) camera (DV420-BU, Andor).

Conflicts of interest

There are no conflicts to declare.

Data availability

The research data underpinning this publication can be accessed at **https://doi.org/10.17630/3d35083e-bdae-43d4-b1b2-f6e47582f7b5**.

Supplementary information (SI) is available. See DOI: **https://doi.org/10.1039/d5mh01275a**.

Acknowledgements

We are grateful to the Engineering and Physical Sciences Research Council of the UK for financial support (grants EP/R035164/1, EP/P010482/1, EP/W015137/1, EP/W007517/1 and EP/Z535291/1). This project has received funding from the European Union's Horizon 2020 research and innovation programme under the Marie Sklodowska-Curie grant agreement no 838885 (NarrowbandSSL). We also acknowledge financial support from the University of St Andrews Restarting Research Funding Scheme (SARRF) which is funded through the Scottish Funding Council grant reference SFC/AN/08/020.

References

1 K. Goushi, K. Yoshida, K. Sato and C. Adachi, *Nat. Photonics*, 2012, **6**, 253–258.
2 H. Kaji, H. Suzuki, T. Fukushima, K. Shizu, K. Suzuki, S. Kubo, T. Komino, H. Oiwa, F. Suzuki, A. Wakamiya, Y. Murata and C. Adachi, *Nat. Commun.*, 2015, **6**, 8476.
3 J. M. Dos Santos, D. Hall, B. Basumatary, M. Bryden, D. Chen, P. Choudhary, T. Comerford, E. Crovini, A. Danos, J. De, S. Diesing, M. Fatahi, M. Griffin, A. K. Gupta, H. Hafeez, L. Hämmerling, E. Hanover, J. Haug, T. Heil, D. Karthik, S. Kumar, O. Lee, H. Li, F. Lucas, C. F. R. Mackenzie, A. Mariko, T. Matulaitis, F. Millward, Y. Olivier, Q. Qi, I. D. W. Samuel, N. Sharma, C. Si, L. Spierling, P. Sudhakar, D. Sun, E. Tankelevičiūtė, M. Duarte Tonet, J. Wang, T. Wang, S. Wu, Y. Xu, L. Zhang and E. Zysman-Colman, *Chem. Rev.*, 2024, **124**, 13736–14110.
4 T. Hatakeyama, K. Shiren, K. Nakajima, S. Nomura, S. Nakatsuka, K. Kinoshita, J. Ni, Y. Ono and T. Ikuta, *Adv. Mater.*, 2016, **28**, 2777–2781.
5 Y. Kondo, K. Yoshiura, S. Kitera, H. Nishi, S. Oda, H. Gotoh, Y. Sasada, M. Yanai and T. Hatakeyama, *Nat. Photonics*, 2019, **13**, 678–682.
6 S. Madayanad Suresh, D. Hall, D. Beljonne, Y. Olivier and E. Zysman-Colman, *Adv. Funct. Mater.*, 2020, **30**, 1908677.
7 H. S. Kim, H. J. Cheon, D. Lee, W. Lee, J. Kim, Y.-H. Kim and S. Yoo, *Sci. Adv.*, 2023, **9**, eadf1388.
8 S. Wu, A. Kumar Gupta, K. Yoshida, J. Gong, D. Hall, D. B. Cordes, A. M. Z. Slawin, I. D. W. Samuel and E. Zysman-Colman, *Angew. Chem., Int. Ed.*, 2022, 61, e202213697.
9 K. Stavrou, L. G. Franca, A. Danos and A. P. Monkman, *Nat. Photonics*, 2024, **18**, 554–561.
10 M. A. Baldo, R. J. Holmes and S. R. Forrest, *Phys. Rev. B*, 2002, **66**, 035321.
11 S. Reineke, K. Walzer and K. Leo, *Phys. Rev. B*, 2007, **75**, 125328.
12 E. B. Namdas, A. Ruseckas, I. D. W. Samuel, S.-C. Lo and P. L. Burn, *Appl. Phys. Lett.*, 2005, **86**, 091104.
13 Y. Zhang, M. Whited, M. E. Thompson and S. R. Forrest, *Chem. Phys. Lett.*, 2010, **495**, 161–165.
14 D. Kasemann, R. Brückner, H. Fröb and K. Leo, *Phys. Rev. B: Condens. Matter Mater. Phys.*, 2011, **84**, 115208.

15 C. Murawski, K. Leo and M. C. Gather, *Adv. Mater.*, 2013, **25**, 6801–6827.
16 F. Montilla, A. Ruseckas and I. D. W. Samuel, *J. Phys. Chem. C*, 2018, **122**, 9766–9772.
17 K. W. Hershey and R. J. Holmes, *J. Appl. Phys.*, 2016, **120**, 195501.
18 K. Masui, H. Nakanotani and C. Adachi, *Org. Electron.*, 2013, **14**, 2721–2726.
19 A. S. D. Sandanayaka, K. Yoshida, T. Matsushima and C. Adachi, *J. Phys. Chem. C*, 2015, **119**, 7631–7636.
20 M. Inoue, T. Serevicius, H. Nakanotani, K. Yoshida, T. Matsushima, S. Jursenas and C. Adachi, *Chem. Phys. Lett.*, 2016, **644**, 62–67.
21 M. Hasan, A. Shukla, V. Ahmad, J. Sobus, F. Bencheikh, S. K. M. McGregor, M. Mamada, C. Adachi, S. C. Lo and E. B. Namdas, *Adv. Funct. Mater.*, 2020, **30**, 202000580.
22 B. S. B. Karunathilaka, U. Balijapalli, C. A. M. Senevirathne, S. Yoshida, Y. Esaki, K. Goushi, T. Matsushima, A. S. D. Sandanayaka and C. Adachi, *Nat. Commun.*, 2020, **11**, 4926.
23 M. Hasan, S. Saggar, A. Shukla, F. Bencheikh, J. Sobus, S. K. M. McGregor, C. Adachi, S. C. Lo and E. B. Namdas, *Nat. Commun.*, 2022, **13**, 254.
24 K. Thakur, B. van der Zee, G. J. A. H. Wetzelaer, C. Ramanan and P. W. M. Blom, *Adv. Opt. Mater.*, 2021, **10**, 2101784.
25 H. S. Kim, S. H. Lee and C. Adachi, *J. Phys. Chem. C*, 2024, **128**, 994–1002.
26 A. Niwa, S. Haseyama, T. Kobayashi, T. Nagase, K. Goushi, C. Adachi and H. Naito, *Appl. Phys. Lett.*, 2018, **113**, 083301.
27 M. Mamada, S. Maedera, S. Oda, T. B. Nguyen, H. Nakanotani, T. Hatakeyama and C. Adachi, *Mater. Chem. Front.*, 2023, **7**, 259–266.
28 D. G. Bossanyi, Y. Sasaki, S. Wang, D. Chekulaev, N. Kimizuka, N. Yanai and J. Clark, *JACS Au*, 2021, **1**, 2188–2201.
29 H. van Eersel, P. A. Bobbert, R. A. J. Janssen and R. Coehoorn, *Appl. Phys. Lett.*, 2014, 105.
30 L. G. King, K. Yoshida and I. D. W. Samuel, *Synth. Met.*, 2024, **301**, 117489.
31 J. C. Ribierre, A. Ruseckas, K. Knights, S. V. Staton, N. Cumpstey, P. L. Burn and I. D. Samuel, *Phys. Rev. Lett.*, 2008, **100**, 017402.
32 S. Diesing, L. Zhang, E. Zysman-Colman and I. D. W. Samuel, *Nature*, 2024, **627**, 747–753.
33 H. C. F. Martens, W. F. Pasveer, H. B. Brom, J. N. Huiberts and P. W. M. Blom, *Phys. Rev. B: Condens. Matter Mater. Phys.*, 2001, **63**, 125328.
34 J. J. M. van der Holst, F. W. A. van Oost, R. Coehoorn and P. A. Bobbert, *Phys. Rev. B: Condens. Matter Mater. Phys.*, 2009, **80**, 235202.

